
BOOSTING THE VALIDITY OF MULTI-CLASS QUANTUM OUTPUTS: LIVING ON THE EDGE

Nathaniel D. Helgesen, Michael Felsberg, Jan-Åke Larsson

Department of Electrical Engineering - Linköping University
Linköping, Sweden, 583 30

{nathaniel.helgesen, michael.felsberg, jan-ake.larsson}@liu.se

ABSTRACT

Quantum machine learning (QML) aims to use quantum computers to enhance machine learning, but it is often limited by the required number of samples due to quantum noise and statistical limits on expectation value estimates. While efforts are made to reduce quantum noise, less attention is given to boosting the quality of the discrete outputs from Variational Quantum Classifiers (VQCs) to reduce the number of samples needed to make confident predictions.

This paper focuses on output representations in multi-class classification, introducing a new mapping of qubit measurements to edges of an n -dimensional simplex, representing independent binary decisions between each pair of classes. We describe this mapping and demonstrate how it offers a direct improvement to the number of valid circuit output samples as well as the accuracy of those outputs over one-hot encoding while advocating for few-sample accuracy as a primary goal for effective VQCs.

Keywords quantum machine learning · sample validity · classification

1 Introduction

As machine learning and quantum computing advance together, researchers are exploring more efficient methods for performing machine learning tasks using quantum computers. One common technique involves parameterized quantum circuits (PQCs), where gate operations on qubits are adjusted through learned parameters, similar to classical machine learning models (Schuld and Petruccione, 2021). Quantum computers are promising for these tasks due to the exponential scaling of quantum state-space, potentially allowing algorithms to perform exponentially faster than classical counterparts—a concept known as *quantum advantage* (Yamakawa and Zhandry, 2024; Nielsen and Chuang, 2010).

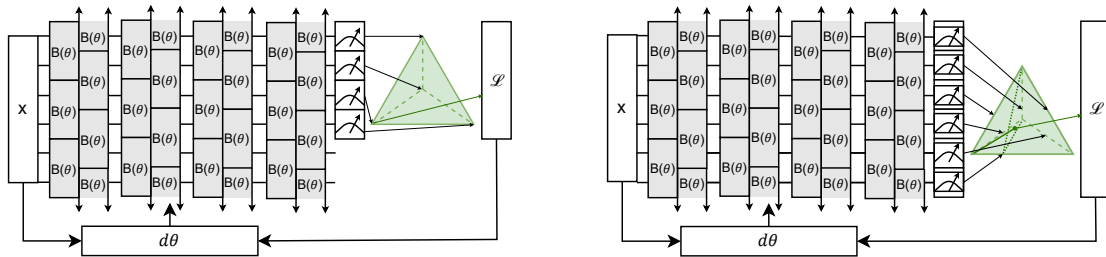


Figure 1: *Left:* Vertex Simplex VQC Training: The number of measured wires is always equal to the number of vertices of the simplex. This number defines the number of wires in both cases. *Right:* Edge Simplex VQC Training: The number of measured wires is always equal to the number of edges of the simplex.

A major challenge to achieving quantum advantage with PQCs is the high number of discrete samples needed to estimate expectation values or state vectors for training and inference. Heisenberg’s uncertainty principle dictates that quantum states cannot be measured exactly, collapsing to a discrete binary state upon measurement (Nielsen and Chuang, 2010). However, the internal state can be approximated by sampling from the PQC multiple times and averaging the discrete outputs (Schuld et al., 2020). PQC algorithms rely on high-fidelity floating-point outputs to calculate cost functions and gradients, necessitating high sampling rates.

The focus on floating-point outputs for gradient calculation has overshadowed the accuracy of discrete samples. We argue that emphasizing accurate discrete outputs will enable finer control over quantum systems and reduce the number of samples needed for inference, bringing QML significantly closer to quantum advantage.

We focus on PQCs for classification, which we distinguish from the more general PQC as variational quantum classifiers (VQCs). Our contributions address two key metrics: the *confidence* of the circuit and the *validity* of its outputs. We define confidence as the proximity of quantum states to computational basis elements before measurement. If qubit expectation values are pushed towards the eigenvalues of the measurement operator, the quantum state aligns closer to the computational basis, increasing the likelihood of these elements appearing upon measurement (Nielsen and Chuang, 2010). We achieve this through non-linear post-processing to control gradient propagation.

Even with perfect confidence, some binary states may be valid while others are meaningless, depending on the output encoding. Most multi-class VQCs use one-hot values as targets (Hur et al., 2022), resulting in the vast majority of states being invalid. To address this, we introduce a new output encoding that reduces the number of invalid states by making some wires unnecessary for class determination. This encoding improves discrete sample accuracy and reduces the number of samples needed for convergence.

To motivate this encoding, we redefine multi-class classification as a series of independent binary decisions which use a voting scheme for confident class predictions. Unlike standard VQC training, which performs loss directly against the circuit outputs, our method treats individual qubit outputs as edges of a $K - 1$ -simplex, where K is the number of classes and simplex vertices. The loss is calculated from distances between a vertex and the intersection point of $K - 2$ -dimensional slices determined by values on its incident edges. The basic premise of this modification is shown in Fig. 1, and the process is detailed in Sec. 3.4.

Previous work has shown that measuring a subset of the input wires is an effective method of avoiding exponentially flat gradient landscapes, known as *barren plateaus* (Cerezo et al., 2024; Leone et al., 2024), however our approach allows effective use of every wire in a VQC. Gradients from our edge method avoid barren plateaus while utilizing every block in the quantum circuits, thus taking a step towards PQCs enabling quantum advantage.

To highlight the importance of model confidence and discrete sample validity in VQC training, in this work we:

- Introduce a new way of looking at discrete VQC outputs that is easily determined and eliminates randomly-selected class predictions
- Outline the training and testing of a novel edge-based simplex representation of VQC outputs which improves on this metric and reduces sampling needs
- Demonstrate an effective non-linear method to control the gradients to VQC parameters and increase sampling accuracy
- Provide comprehensive results of these methods as compared to the nearly-standard one-hot encoding
- Show experimentally that our edge method is able to avoid barren plateaus while balancing the spread of gradient propagation throughout the quantum circuits.

2 Related Work

Quantum Machine Learning (QML) has been around for just over a decade (Lloyd et al., 2013), though it has gained massive momentum since then. Various classical machine learning algorithms, including generative adversarial algorithms (Hamilton et al., 2019; Benedetti et al., 2019), support vector machines (Li et al., 2022; Park et al., 2020; Rebertrost et al., 2014), Bayesian networks (Du et al., 2018; Gao et al., 2022; Borujeni et al., 2021; Zhao et al., 2019), and convolutional neural networks (Hur et al., 2022; Cong et al., 2019; Liu et al., 2021; Bokhan et al., 2022), have been adapted for quantum computing, often matching or surpassing classical performance. Many of these methods benefit from having fewer parameters and comparable accuracy to their classical counterparts.

Parameterized quantum circuits (PQCs), wherein rotation gate angles are optimized similarly to classical machine learning (McClean et al., 2016; Cong et al., 2019), are a key technique in the field, enabling many of the aforementioned quantum adaptations as well as other algorithms aiming to solve problems beyond the reach of classical computers. The

Quantum Approximate Optimization Algorithm (QAOA) was designed to perform high-dimensional combinatorial optimization (Farhi et al., 2014) and Variational Quantum Eigensolvers (VQEs) is a promising tool for answering previous intractable questions in quantum chemistry (Tilly et al., 2022). Both of these tools show promise toward the strive for quantum advantage (Feynman, 2018; Manin, 1980; Preskill, 2012), yet a few challenges remain that are separate from the algorithms themselves.

Many researchers focus on overcoming major obstacles in the field such as error correction (Lidar and Brun, 2013; Devitt et al., 2013; Chiaverini et al., 2004) and barren plateaus (Cerezo et al., 2021b, 2024; Zhao and Gao, 2021; Liu et al., 2022; Letcher et al., 2024), which both stem from the high noise in the quantum computers of today and limit the effectiveness of otherwise advantageous quantum algorithms. These challenges affect quantum computing as a whole and are thus important to understand and solve, yet another limitation has always existed that receives much less attention.

A significant challenge in achieving quantum advantage with PQCs is the high sampling rate required to estimate expectation values due to Heisenberg’s uncertainty principle (Schuld and Petruccione, 2021; Nielsen and Chuang, 2010). To highlight this issue, we focus on supervised learning on the task of classification, as this task was one of the fundamental milestones in classical machine learning (Quinlan, 1986; Rumelhart et al., 1986; LeCun et al., 1998; Saraswat, 2021).

Supervised QML can be done in several ways. Multi-class classification is often performed by using PQC as a layer in a classical machine learning model, also known as a hybrid model, which has shown promising results in research done by Chalumuri et al. (2021), Jing et al. (2022), Liu et al. (2021), Senokosov et al. (2024), Shi et al. (2023), and Stein et al. (2022), but typically relies on using floating outputs from the circuit. Acquiring floating point values from a quantum computer requires it to either be simulated or sampled many times so values that can be used to calculate gradients can be obtained or estimated, respectively. While these strategies work, they do not lend themselves toward quantum advantage, since simulation is classical and the sampling needs when using quantum hardware can grow anywhere from linearly to exponentially, depending on the circuit (Cerezo et al., 2021b, 2024; Gao et al., 2022).

In this paper we opt to use the PQC as the classifier itself. This has been done several times before by Bokhan et al. (2022), Hur et al. (2022), Shen et al. (2024), Stein et al. (2022), and Zhou et al. (2023), however, to the best of our knowledge, this is rarely done for more than 2 classes, and it tends to struggle from the same problem as in hybrid methods. Previous work tends to use maximums and thresholds against the floating-point outputs to determine if the output from the PQC was correct. This process, once again, requires many samples to estimate. It is our primary intention to demonstrate that moving the goalpost from accurate expectation values to accurate samples is possible and worthwhile through performing multi-class classification in a non-hybrid PQC, with the underlying goal of moving the field toward quantum advantage.

3 Method

Our approach to few-samples-based VQCs is based on the idea of replacing the full multinomial classifier with sub-problems. These sub-problems are derived from a geometric perspective of the original problem induced by the one-hot vector outputs, represented by a $K - 1$ -simplex. One common method of doing multi-class classification with a VQC is to treat each qubit as the logit for a single class (Stein et al., 2022; González et al., 2020; Nghiem et al., 2020). We refer to this as the vertex method, because this correlates geometrically to mapping the outputs of the circuit to the vertices of the $K - 1$ -probability simplex.

For our edge representation, the outputs of the VQC are first mapped to the edges of the same simplex, and the edges incident to each vertex are used to calculate a logit for that vertex. When looking at the discrete case, this mapping causes a two-fold increase in the probability of the model guessing the correct class, even prior to training. This is because, for the vertex encoding, there is always exactly one correct answer in the 2^K -dimensional space, meaning the correct answer would be chosen with a probability of 2^{-K} . For the edge method, $K - 1$ of the $W = \binom{K}{2}$ edges are irrelevant to classifying a particular example, meaning that the correct answer happens when all incident edges are in accord, which comes at a probability of $2^{-(K-1)}$, or twice as likely. Our results in Sec. 4.1 show that this effect is greatly magnified by training as K increases. In Section 3.4, we will go over how to calculate the predictions in our edge method and use them to train the VQC.

The number of qubits that need to be measured for the vertex method is K , which means that for class counts, $K > 3$, the vertex method uses the measurements from only a subset of the qubits, whereas the edge method uses all of the qubits. Measuring a subset of the wires is standard practice in VQC training (Hur et al., 2022; Bokhan et al., 2022; Zhou et al., 2023; Shen et al., 2024; Stein et al., 2022), and has been shown to be an effective means of avoiding barren plateaus (Cerezo et al., 2021b; Leone et al., 2024; Cerezo et al., 2024).

For consistency with regard to the number of features encoded into the VQC and to leverage the reduced output space which was shown by Leone et al. (2024) to reduce barren plateaus, both methods use the same number of qubits $W = \binom{K}{2}$. This W is identically the number of edges in the $K - 1$ -simplex. Input encoding and circuit design are discussed in Sec. 3.2.

Both the vertex representation and our edge representation are trained under simulation against a target value that is encoded as a one-hot vector. Encoding an integer y as a one-hot vector means replacing the integer class-label with $e^{(y)}$. Under inference, we look at both the discrete (pseudo-random) sample outputs and the simulated expectation values to get a full-picture understanding of the two encoding methods.

3.1 Computational Tools

All experiments were performed using the Python packages JAX (Bradbury et al., 2018) and PennyLane (Bergholm et al., 2022). JAX is an auto-differentiation package that enables the computation of gradients for machine learning models and just-in-time compilation for highly parallel processes such as batched VQC operations. PennyLane is a superconducting quantum computing package for Python that interfaces with most modern superconducting quantum computer APIs and machine learning packages, including JAX, which enables rapid training and testing of the VQCs used in this work. Experiments were performed under CPU simulation.

3.2 Circuit Design

Based on its consistently positive results in the work of Hur et al. (2022), the dual angle encoding method is used to encode the image information as the first step in the circuit. This means that the number of features that can be encoded into the circuit will always be $2W$, or double the number of qubits, W , with half of the information encoded with Pauli-X rotations, and the other half with Pauli-Y rotations. The data to be encoded is limited to the range $[0, \pi]$ to ensure unique embeddings. Lowering the dimensionality of the input data from the to $2W$ features is done by a multilayer perceptron-based autoencoder with dropout (Bishop, 2006).

All experiments use a 2-design qubit ring structure (Cerezo et al., 2021b) wherein each qubit, referred to as *wires* in the context of sequential gate operations, is connected with its two neighboring wires via alternating rings of computational blocks (and the first and last wires are neighbors). A computational block consists of parameterized Pauli rotations and 2-qubit controlled operations. Two of the blocks - CNN7 and CNN8 - were originally created by Sim et al. (2019) and modified to work well in this kind of 2-design by Hur et al. (2022). The SO(4) and SU(4) blocks were suggested by Wei and Di (2012) and Vatan and Williams (2004), respectively, and also modified by Hur et al. (2022). The Strongly Entangling Layers block was created by Schuld et al. (2020) and we test it with both CNOT and controlled Pauli-Z as the imprimitive 2-qubit gates. Four layers of rings were used for all tests, though this can be increased to make the circuits more expressive. To produce samples and expectation values, qubits were measured in the Pauli-Z basis.

We present our main results as averages over all six block types for the two datasets and $K \in \{3, 4, 5, 6\}$. All permutations were performed using the same five random seeds for consistency in comparison, leading to a total of 240 models (excluding those trained for ablations) each trained using both methods. In the case that some circuits perform better in spite of worse averages, we also present the percentage of circuits that achieve better performance using each method per metric.

3.3 Non-Linear Normalization

In both cases, the expectation values from the VQC are transformed using a sigmoid function in a process we call *tempering*, inspired by soft-thresholding (13) from Felsberg et al. (2009). This tempering reverses the monotonicity of the data and normalizes it, which both need to be done since the expectation value range for a quantum Pauli measurement is $[-1, 1]$, and expectation values of -1 and 1 are commonly used to represent a binary 1 and 0, respectively (Nielsen and Chuang, 2010; Schuld and Petruccione, 2021). Transforming expectation values this way enables us to reason about them as the probabilities that their qubits, when discretized through measurement, will output 1 as opposed to 0.

The secondary goal in applying such a function is to ensure that the gradients returning to the circuit are minimal near expectation values of -1 and 1 , and maximal near 0, since expectations near the extrema are more likely to discretize to either 1 or 0, respectively, and expectation values of 0 operate like coin-flips when discretized. Vanishing gradients from the sigmoid function have been a large enough problem in classical machine learning for them to be considered outdated (Ven and Lederer, 2021; Roodschild et al., 2020), but in this use case, it provides exactly the behavior we want. Originally, the logistic function was chosen due to the ease of calculating its gradient (Goyal et al., 2020), which, while efficient, may not lead to the optimal training behavior in quantum circuits.

There are many functions which have the required shape, with the biggest difference between them being their domains relative to their asymptotes and none reaching diminished gradients in the domain $[-1, 1]$. Because of this, the inputs to the functions need to be scaled to make full use of this vanishing effect. This scaling can be such that the minimum gradient returning to the circuit is arbitrarily close to 0, but the more this scaling is applied, the more of the input domain receives very little gradient, as shown in Fig 2. In this study, we ablated over three sigmoid like functions - namely, the logistic function, the error function, and the Gudermannian function (Gambini et al., 2024) - and two minimum gradient levels for each - namely, 0.01 and 0.001. To calculate the scaling, we simply find the input value to the first derivative of each function that gives the minimum value we set.

The primary results of this work are gathered using the best performing combination in the ablation, which was the error function with a minimal gradient of 0.01.

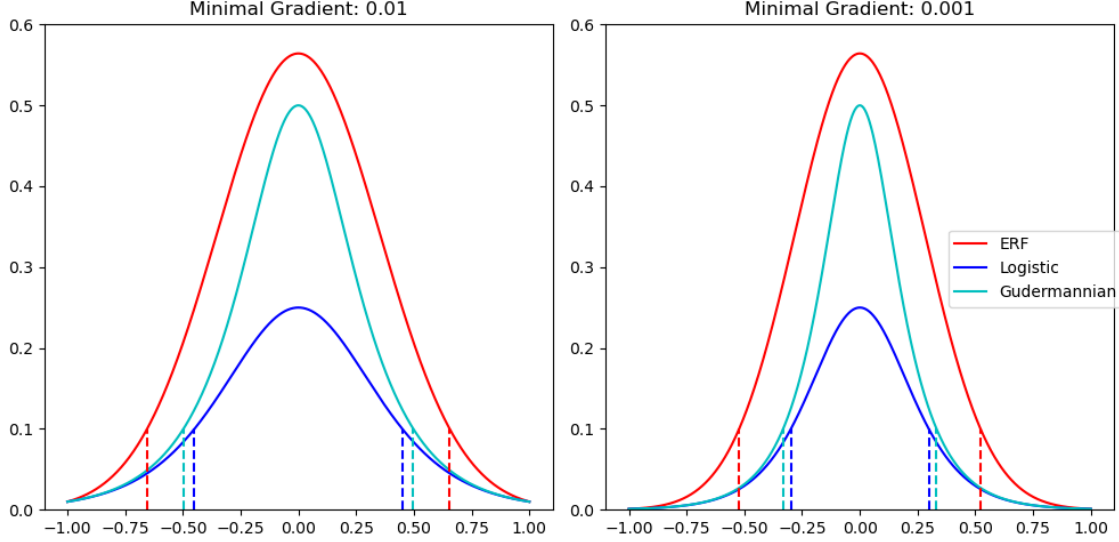


Figure 2: Plots of the derivatives of the tempering functions after being scaled such that the chosen minimal gradient occurs at -1 and 1. Dashed lines showing where each function has a gradient value of 0.1, which illustrates the relative decrease in gradient scale between the three functions. Due to scaling the functions such that they have equivalent minimum values, the graphs are equal at their endpoints, but it can be seen that the logistic and Gudermannian functions have smaller gradients which also vanish sooner than in the error function (ERF).

3.4 Edge Representation Training Method

This section will define how to train a VQC using an edge representation. For visual reference, diagrams of the process in the $K = 3$ and $K = 4$ cases, where K is the number of classes, are shown in Fig. 3, respectively. All training for both the edge and vertex methods is performed using the expectation values of the circuit under ideal simulation.

The goal of our method is to output edge values, which represent binary decisions between K classes, on each of the $W = \binom{K}{2}$ qubits, and then to convert them into K individual decisions. To strike a good balance between the model outputting confident values in the range $[0, 1]$ and having quality gradients when the values are close to 0 or 1, non-linear normalization tempers the circuit outputs prior to calculating the predictions.

Each tempered value is treated as a distance along an edge e_{ij} between two vertices, \mathbf{v}_i and $\mathbf{v}_j: i, j \in \{1, \dots, K\}, i < j$, on a regular 0-centered $K - 1$ -simplex. The coordinates of the vertices of the regular 0-centered simplex are precalculated and used during training to calculate the coordinates of the edge vectors \mathbf{e}_{ij} from the edge values e_{ij} as,

$$\mathbf{e}_{ij} = (1 - e_{ij})\mathbf{v}_i + e_{ij}\mathbf{v}_j, \quad (1)$$

For each vertex, \mathbf{v}_i , there will be $K - 1$ incident edges. For each of these edge vectors, \mathbf{e}_{ij} , there are $K - 2$ vertices that are not an endpoint of the edge, $\mathbf{v}_k: k \in \{1, \dots, K\} \setminus \{i, j\}$. These \mathbf{v}_k form a $(K - 2)$ dimensional hyperplane, or slice with \mathbf{e}_{ij} , which has normal vector \mathbf{s}_{ij} , calculated as,

$$\mathbf{s}_{ij} = \left(\text{span}(\mathbf{v}_k - \mathbf{e}_{ij})_{k \neq i, j} \right)^\perp. \quad (2)$$

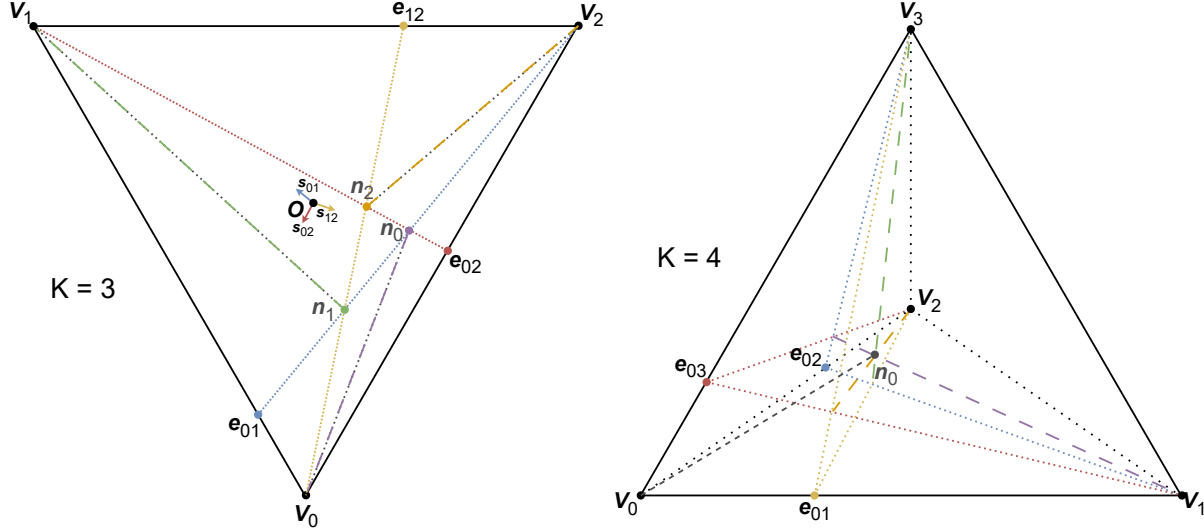


Figure 3: *Left*: Geometric visualization of solving for each \mathbf{n}_i with the edge method when $K = 3$. Best viewed in color. *Right*: Geometric visualization of solving for \mathbf{n}_0 with the edge method when $K = 4$. In this diagram, the s_{ij} are left unmarked, however they would be vectors pointing from the origin in a direction perpendicular to the 3-planes which intersect at \mathbf{n}_0 . Best viewed in color.

Given the guarantees that none of the slices are orthogonal or parallel and the fact that there will always be $K - 1$ of them in $K - 1$ dimensional space, the slices will always have exactly one point of intersection, \mathbf{n}_i , which can be found by solving the linear system of equations

$$(\mathbf{n}_i - \mathbf{e}_{ij}) \cdot \mathbf{s}_{ij} = 0, \quad \forall j, \quad (3)$$

and the final model predictions are then,

$$p_i = 1 - \|\mathbf{v}_i - \mathbf{n}_i\|^2. \quad (4)$$

Using the predictions p_i , a loss is calculated and used to find the gradients of the VQC parameters using standard backpropagation. The MSE-loss is computed against the values y_i of the one-hot targets y for each element b in the mini-batch of size B , as

$$\mathcal{L} = \frac{\sum_b \sum_i (p_i - y_i)^2}{BK}. \quad (5)$$

One major strength of this method is that it calculates K partially independent point masses in the probability simplex rather than the single effective point mass determined by assigning outputs to vertices. Though both MSE-loss and cross-entropy have been shown to work similarly well by Hur et al. (2022), MSE was chosen because the partial derivatives of each individual logit are separated by the sum, preserving this beneficial effect, unlike in cross-entropy which requires soft-max to be performed and thus treats the individual values dependently.

Under discrete inference, binary outputs from the model trained using this method are not transformed, but are rather used to predict by comparing them with the binary string representative of the target class. In these binary strings,

$$e_{ij} = 0 \iff i < j \quad (6)$$

on the incident edges e_{ij} for vertex v_i , with the rest of the edges e_{jk} being free elements. If all the e_{ij} for a given v_i agree, the predicted class for that binary string is determined to be i , but if no i can be assigned, then the prediction is considered invalid.

3.5 Gradient Balancing

In many classification tasks, input data has a higher dimensionality than output data, leading to VQCs which have more wires than are required on the output. As the difference between the number of input and output wires grows, so too does the scale of the *light-cone* effect, wherein the VQC parameters not part of gates in the backwards light-cone stemming from the measured wires receive no gradients, as shown by Leone et al. (2024) and Cerezo et al. (2024).

In Fig. 4, this effect is visualized for $K = 5$ wherein measurement wires are assigned the value 1, ignored wires are assigned values 0, and blocks are assigned luminance values depending on the total luminance back-propagating from

their outputs. In this way, the imbalanced gradient flow is visualized. The figure demonstrates how this light-cone effect further leads to reduced and imbalanced gradients closer to the inputs of the VQC.

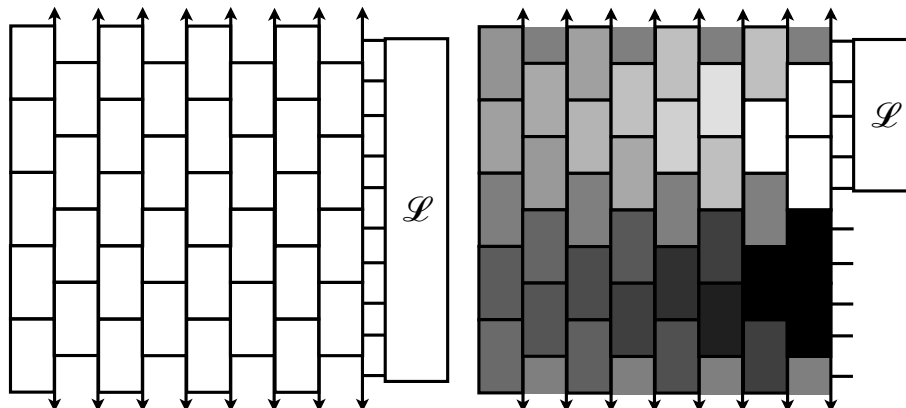


Figure 4: Diagram showing the relative flow of gradients through 4-layer 2-qubit ring structure VQC with $K = 5$ and thus $\binom{5}{2} = 10$ wires. Lighter blocks receive more gradient. Left: Using the edge method, every block receives gradients from every pass of the training. Right: Using the Vertex method, when $K \geq 5$ some wires are completely ignored which leads to an uneven spread of gradients throughout the circuit, including several blocks where no gradients are received at all.

Not only is this an inefficient use of available blocks that scales proportionally to the number of wires, it also has the effect of prioritizing the inputs unevenly and arbitrarily. This can be canceled by adding more layers to the network, though this quickly becomes intractable both in simulation and on the noisy intermediate-scale quantum hardware of today.

The light-cone setup has been shown by Hur et al. (2022) and Cerezo et al. (2021a) to be a useful paradigm in training VQCs without exponentially vanishing gradients. Because our method is setup such that a different subset of the wires are irrelevant for each class, our method also manages to avoid barren plateaus. Rather than reducing the set of measured qubits to the same consistent subset, our method reduces to per-class subsets of wires to make use of every parameter in the model, and thus improves expressibility and gradient balance without exponentially vanishing gradients.

We provide example charts of gradient spread averaged over all training runs when $K = 5$ for both the edge and vertex cases and discuss this effect in greater detail in Sec. 4.4.

4 Results

To test the efficacy of the edge representation as well as to ablate over the decisions made to support the training procedure, a grid test over several datasets, hyperparameters, and block circuits was performed. Tests were done on both the MNIST Digits dataset (LeCun et al., 1998) and the MNIST Fashion dataset (Xiao et al., 2017), with five random subsets of K -classes. The same five random subsets were used for each experiment with additional classes chosen from the remaining digits as K increases.

This led to a total of 10 data sets, which each were trained for every block with $K \in \{3, \dots, 6\}$. The models were trained with a batch size of 32 for 6 epochs using the Adam optimizer using an exponential decay learning rate scheduler with a starting learning rate of 0.01, a decay rate of 0.9, and scheduler steps equal to one-tenth of the total training steps (Kingma and Ba, 2017). This process was determined using an ablation provided in Sec. 6.

For clarity, in this section we will use the affixes "t-" and "m-" to separate testing and measurement, respectively. Confusion arises naturally when talking about samples and predictions, given both the individual elements of the test-set and the discrete outputs from the VQC are commonly referred to as *samples*, and the labels attached to the test-set elements and the predictions from the VQC are designated by *classes*.

To calculate sample accuracies, a confusion matrix was built by adding one to the class which was chosen most among all of the m-samples in the row of the t-class for each t-sample, meaning the micro accuracy C_m for the full test set is the percentage of t-samples which were correctly guessed by the majority of the m-samples generated by the circuit, and is calculated as ratio of the trace of the matrix to the total t-samples. A full table including both the micro and macro accuracies is shown in Sec. 7.

Dataset	K	Edge				Vertex			
		C_r (%)	C_m (%)	T_r (%)	T (%)	C_r (%)	C_m (%)	T_r (%)	T (%)
Fashion	3	100.00	73.78	50.00	76.35	0.00	54.96	50.00	76.27
Fashion	4	100.00	59.22	16.67	81.44	0.00	24.29	83.33	82.02
Fashion	5	83.33	20.37	16.67	69.30	16.67	4.02	83.33	70.04
Fashion	6	83.33	4.61	33.33	65.12	16.67	0.24	66.67	66.42
Digits	3	100.00	70.90	100.00	76.12	0.00	45.55	0.00	75.19
Digits	4	100.00	58.51	16.67	86.30	0.00	20.38	83.33	87.24
Digits	5	83.33	14.33	33.33	69.26	16.67	1.12	66.67	68.59
Digits	6	83.33	3.23	33.33	66.50	16.67	0.05	66.67	67.29

Table 1: Side by side comparison of the results of the constant sampling rate experiments on all 240 permutations averaged over the circuits and 5 training rounds, as defined in Sec. 3.2. Threshold accuracy T shows a small difference between the two training methods when a marginal is taken over individual wires. Micro accuracy m demonstrates a big difference when discrete binary output strings are used rather than marginals.

We analyze the efficacy of our edge method using two sets of metrics. The first set begins by counting invalid predictions as a separate class and drawing 100 m-samples for each t-sample. The confusion matrix calculated this way includes an extra column for invalid samples - which are not discarded in this process - and are thus not included in the trace, but are included in the total when calculating C_m . We discuss the results of this constant sampling rate test in Sec. 4.1.

We also include the threshold accuracy T in this set. Threshold accuracy is given by the highest floating point activation from the simulated circuits and determined by comparing the target class to the tempered expectation values in the vertex case and from the simplex-mapped tempered expectation values in the edge case. This value is not significantly different between the methods and is presented to show a lack of detrimental effects from the edge case relative to the standard vertex case.

The second set was calculated by drawing m-samples until the null hypothesis that the m-samples were drawn iid could be rejected using a χ^2 -significance test on V_m with an α -value of .001, and keeping the matrix and accuracy from that m-sample count. The number of m-samples from this process is reported as the sample size S , which we provide a spread of in Sec. 4.2 alongside the kept V_m .

Due to the large number of circuits and datasets tested on, the reported metrics are averaged over the six circuit block variants. We include the average ranking r for each metric as well, which is calculated as the percentage of circuit blocks which scored better for that training method. The random seeds for each run are kept consistent so as to leave nothing to chance and truly assess the quality of the VQCs trained using each method.

In Section 4.3, we provide quantitative evidence for our use of non-linear normalization, and in Section 4.4, we provide quantitative evidence of the insight provided in Section 3.5.

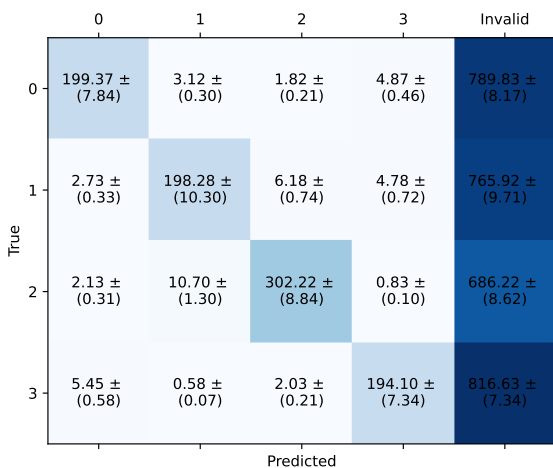


Figure 5: Confusion matrix for $K = 4$ over all circuits trained using the vertex method. Each cell displays the average and standard error of t-samples that were majority selected by all 100 m-samples.

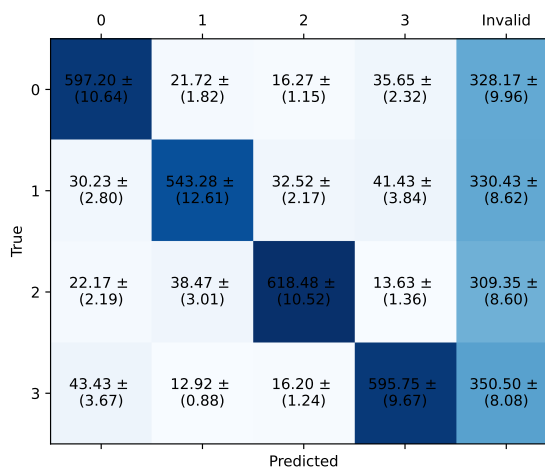


Figure 6: Confusion matrix for $K = 4$ over all circuits trained using the edge method. Each cell displays the average and standard error of t-samples that were majority selected by all 100 m-samples.

4.1 Constant Sampling Rate

In Tab. 1, we compare the edge and vertex methods in terms of the standard threshold accuracy T as well as the micro sampling accuracy C_m when a constant sampling rate is chosen. For consistency, we keep this sampling rate at 100. The threshold accuracy is a marginal over individual wires that is agnostic to the discrete binary output strings. Because of this, it can hide the frequency with which invalid binary strings are output by a VQC to the extent that, if it is used as the only metric, the two methods presented in this paper would appear to be approximately equivalent.

This is, however, not the case when looking at the average C_m for each method. It can be seen that as K goes up, the difference in C_m performance between the edge and vertex methods goes up, until at $K = 6$ it is around several orders of magnitude more accurate. Confusion matrices averaged over all circuits and datasets for $K = 4$ are shown in Fig. 5 and Fig. 6 for the vertex and edge methods, respectively. It can be easily seen by comparing the two that a much larger number of invalid m-samples are produced in the vertex case, which leads to the higher C_m values in Tab. 1.

Dataset	K	Edge				Vertex			
		V_r (%)	V_m (%)	S_r (%)	$S \downarrow$	V_r (%)	V_m (%)	S_r (%)	$S \downarrow$
Fashion	3	50.00	74.61	66.67	447.50	50.00	75.12	33.33	456.80
Fashion	4	16.67	77.11	83.33	597.73	83.33	77.85	16.67	659.50
Fashion	5	33.33	66.25	66.67	440.77	66.67	66.24	33.33	434.57
Fashion	6	33.33	57.66	66.67	197.17	66.67	58.12	33.33	229.80
Digits	3	66.67	72.23	33.33	295.43	33.33	71.61	66.67	284.80
Digits	4	16.67	83.53	83.33	1222.83	83.33	83.45	16.67	1408.63
Digits	5	33.33	66.76	66.67	349.13	66.67	65.94	33.33	453.10
Digits	6	50.00	60.59	83.33	209.73	50.00	60.14	16.67	289.37

Table 2: Side by side comparison of the results of the valid sampling experiments on all 240 permutations averaged over the circuits and 5 training rounds, as defined in Sec. 3.2. Micro accuracy m shows the average micro accuracy achieved after measuring a convergent number of circuit runs. The average number of m-samples needed to converge is shown as S .

4.2 Valid Sampling Count

In Tab. 2, we further compare the edge and vertex methods abilities to output quality samples by ignoring invalid samples until the micro accuracy V_m over valid samples converges. Taking this convergence as a stopping point allows for comparison regarding the necessary number of m-samples needed to be drawn from a trained circuit. It can be seen that both training methods converge around the same V_m values, yet the edge method often requires considerably less m-samples to get to that point.

Though S does not improve at the same rate as C_m , it does show a gradual divergence as K increases.

4.3 Normalization Ablation

We performed our ablation process on the CNN7 block from Sim et al. (2019) using $K = 4$ on the MNIST Digits dataset. We compared ERF, Gudermannian, and the logistic function at minimal gradient values of 0.01 and 0.001, as well as a linear monotonicity reversing normalization.

The scores presented in Tab. 3 are Friedman-scores computed over a range metrics: the micro and macro accuracies computed as in both the constant and valid sampling experiments, the threshold accuracy and the log-likelihood ratio computed as a difference between the highest and second-highest activation class, and the sampling rate from the valid sampling experiments. We use the Friedman-scores to decide on the best tempering method without focusing on a single metric.

Function	ERF		Linear		Logistic		Gudermannian	
Min Grad	0.01	0.001	0.01	0.001	0.01	0.001	0.01	0.001
F-Score \uparrow	5.125	4.5	4.125	4.125	4.625	4.25	4.375	4.125

Table 3: Averaged Friedman rank over all relevant statistics on CNN7 with $K = 4$ using the edge method. Highest score was chosen as the optimal.

4.4 Gradient Flow

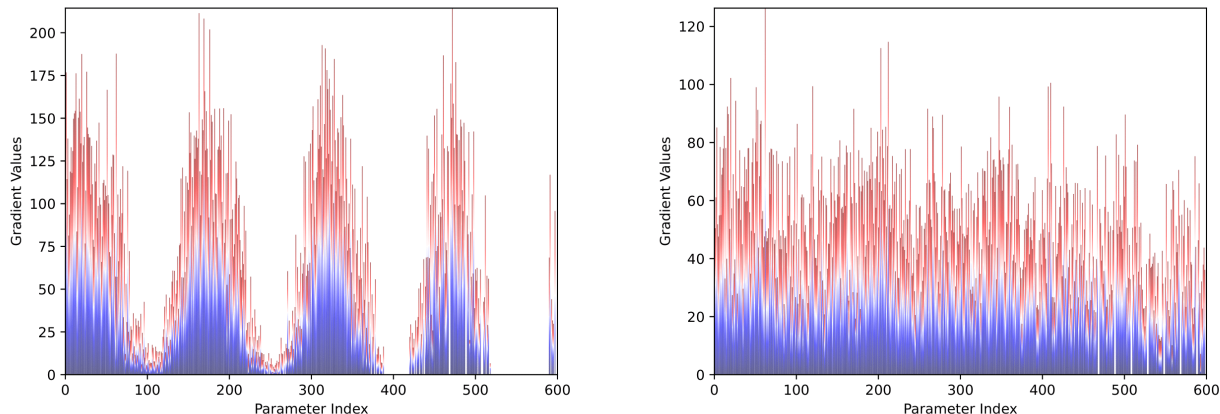


Figure 7: *Left*: Gradient totals for Vertex training, note the rather steep differences in total gradients as well as the numerous parameters which receive no gradients at all. *Right*: Gradient totals for Edge training. While there are still peaks, the overall variance in the gradients is much lower than the vertex case, and there are no parameters which receive zero gradient.

As discussed in Sec. 3.5, training using the edge representation also has a balancing effect on gradients. In Fig. 7, we display the total gradients received by each parameter during 6 epochs of training with $K = 6$ on the CNN7 block for the vertex and edge case, respectively. Both charts have peaks at parameters used in the two qubit gates within their blocks, as with these it is possible to be the partial derivative of twice as many later parameters.

The strong dips in gradients in the vertex case are caused by the reverse light-cone effect caused by unused wires on the output, which can be seen especially clearly in the patch around index values 550 where no gradients are received. This subset of the parameters are those that parameterize the blocks directly preceding the unmeasured wire outputs. Eventually the gradients begin to add up in the gates on those wires due to the connections with wires that have received gradients, though this is always decreased because of the reverse light-cone effect.

The edge method does not have this problem, and thus every gate is necessary and useful, likely leading to the consistent validity and decreased sampling needs among circuits trained in this manner. It is noteworthy that many of the spikes in the edge method correlate with gaps in the vertex case, in spite of identical inputs and random seeds, possibly meaning that important information transfer among the wires is lost because of this light-cone effect.

5 Conclusions

In this paper, we take the first step toward improving the accuracy of discrete outputs from Variational Quantum Classifiers. Achieving this goal has broader implications for quantum machine learning, as reducing sampling requirements removes a significant obstacle to quantum computers outperforming classical computers in efficiency.

Our findings, supported by experiments, highlight a novel direction in quantum machine learning. We focus on designing models that yield valid and accurate discrete outputs more often by leveraging the high-dimensional Hilbert space provided by quantum computers.

To achieve this, we propose a classical post-processing method for VQCs that maps the output space to a regular simplex, resulting in a constant increase in valid and accurate discrete samples. While enhancing model robustness is beneficial for inference, training models to produce more confident outputs requires adjustments to the standard training procedure. We compare our approach with a common VQC that produces one-hot results and demonstrate how our simplex method remains superior. Overall, our results are a major leap toward highly confident and accurate discrete outputs.

References

- Marcello Benedetti, Delfina Garcia-Pintos, Oscar Perdomo, Vicente Leyton-Ortega, Yunseong Nam, and Alejandro Perdomo-Ortiz. A generative modeling approach for benchmarking and training shallow quantum circuits. *npj Quantum Inf*, 5(1):45, 2019.
- Ville Bergholm, Josh Izaac, Maria Schuld, Christian Gogolin, Shahnawaz Ahmed, Vishnu Ajith, M. Sohaib Alam, Guillermo Alonso-Linaje, B. AkashNarayanan, Ali Asadi, Juan Miguel Arrazola, Utkarsh Azad, Sam Banning, Carsten Blank, Thomas R

- Bromley, Benjamin A. Cordier, Jack Ceroni, Alain Delgado, Olivia Di Matteo, Amintor Dusko, Tanya Garg, Diego Guala, Anthony Hayes, Ryan Hill, Aroosa Ijaz, Theodor Isaacsson, David Ittah, Soran Jahangiri, Prateek Jain, Edward Jiang, Ankit Khandelwal, Korbinian Kottmann, Robert A. Lang, Christina Lee, Thomas Loke, Angus Lowe, Keri McKiernan, Johannes Jakob Meyer, J. A. Montañez-Barrera, Romain Moyard, Zeyue Niu, Lee James O’Riordan, Steven Oud, Ashish Panigrahi, Chae-Yeun Park, Daniel Polatajko, Nicolás Quesada, Chase Roberts, Nahum Sá, Isidor Schoch, Borun Shi, Shuli Shu, Sukin Sim, Arshpreet Singh, Ingrid Strandberg, Jay Soni, Antal Száva, Slimane Thabet, Rodrigo A. Vargas-Hernández, Trevor Vincent, Nicola Vitucci, Maurice Weber, David Wierichs, Roeland Wiersema, Moritz Willmann, Vincent Wong, Shaoming Zhang, and Nathan Killoran. Pennylane: Automatic differentiation of hybrid quantum-classical computations, 2022.
- Christopher M Bishop. Pattern recognition and machine learning. *Springer google schola*, 2:1122–1128, 2006.
- Denis Bokhan, Alena S. Mastiukova, Aleksey S. Boev, Dmitrii N. Trubnikov, and Aleksey K. Fedorov. Multiclass classification using quantum convolutional neural networks with hybrid quantum-classical learning. *Front. Phys.*, 10:1069985, 2022. arXiv:2203.15368 [quant-ph].
- Sima E. Borujeni, Saideep Nannapaneni, Nam H. Nguyen, Elizabeth C. Behrman, and James E. Steck. Quantum circuit representation of Bayesian networks. *Expert Systems with Applications*, 176:114768, 2021.
- James Bradbury, Roy Frostig, Peter Hawkins, Matthew James Johnson, Chris Leary, Dougal Maclaurin, and Skye Wanderman-Milne. Jax: Composable transformations of python+numpy programs, 2018.
- M. Cerezo, Andrew Arrasmith, Ryan Babbush, Simon C. Benjamin, Suguru Endo, Keisuke Fujii, Jarrod R. McClean, Kosuke Mitarai, Xiao Yuan, Lukasz Cincio, and Patrick J. Coles. Variational Quantum Algorithms. *Nat Rev Phys*, 3(9):625–644, 2021a. arXiv:2012.09265 [quant-ph, stat].
- M. Cerezo, Akira Sone, Tyler Volkoff, Lukasz Cincio, and Patrick J. Coles. Cost function dependent barren plateaus in shallow parametrized quantum circuits. *Nat Commun*, 12(1):1791, 2021b. Publisher: Nature Publishing Group.
- M. Cerezo, Martin Larocca, Diego García-Martín, N. L. Diaz, Paolo Braccia, Enrico Fontana, Manuel S. Rudolph, Pablo Bermejo, Aroosa Ijaz, Supanut Thanasilp, Eric R. Anschuetz, and Zoë Holmes. Does provable absence of barren plateaus imply classical simulability? Or, why we need to rethink variational quantum computing, 2024. arXiv:2312.09121 [quant-ph, stat].
- Avinash Chalumuri, Raghavendra Kune, and B. S. Manoj. A hybrid classical-quantum approach for multi-class classification. *Quantum Inf Process*, 20(3):119, 2021.
- John Chiaverini, Dietrich Leibfried, Tobias Schaetz, Murray D Barrett, RB Blakestad, Joseph Britton, Wayne M Itano, John D Jost, Emanuel Knill, Christopher Langer, et al. Realization of quantum error correction. *Nature*, 432(7017):602–605, 2004.
- Iris Cong, Soonwon Choi, and Mikhail D. Lukin. Quantum convolutional neural networks. *Nat. Phys.*, 15(12):1273–1278, 2019. Number: 12 Publisher: Nature Publishing Group.
- Simon J Devitt, William J Munro, and Kae Nemoto. Quantum error correction for beginners. *Reports on Progress in Physics*, 76(7):076001, 2013.
- P Kingma Diederik. Adam: A method for stochastic optimization. (*No Title*), 2014.
- Yuxuan Du, Tongliang Liu, and Dacheng Tao. Bayesian Quantum Circuit, 2018. arXiv:1805.11089 [quant-ph].
- Edward Farhi, Jeffrey Goldstone, and Sam Gutmann. A Quantum Approximate Optimization Algorithm, 2014. arXiv:1411.4028 [quant-ph].
- Michael Felsberg, Sinan Kalkan, and Norbert Krüger. Continuous dimensionality characterization of image structures. *Image and Vision Computing*, 27(6):628–636, 2009.
- Richard P Feynman. Simulating physics with computers. In *Feynman and computation*, pages 133–153. CRC Press, 2018.
- Milton Friedman. The use of ranks to avoid the assumption of normality implicit in the analysis of variance. *Journal of the American Statistical Association*, 32(200):675–701, 1937.
- Alessandro Gambini, Giorgio Nicoletti, and Daniele Ritelli. A structural approach to gudermannian functions. *Results in Mathematics*, 79(1):10, 2024.
- Xun Gao, Eric R. Anschuetz, Sheng-Tao Wang, J. Ignacio Cirac, and Mikhail D. Lukin. Enhancing Generative Models via Quantum Correlations. *Phys. Rev. X*, 12(2):021037, 2022. arXiv:2101.08354 [cond-mat, physics:quant-ph, stat].
- Fabio A González, Vladimir Vargas-Calderón, and Herbert Vinck-Posada. Supervised learning with quantum measurements. *arXiv preprint arXiv:2004.01227*, 2020.
- Mohit Goyal, Rajan Goyal, P Venkatappa Reddy, and Brejesh Lall. Activation functions. *Deep learning: Algorithms and applications*, pages 1–30, 2020.
- Priya Goyal, Piotr Dollár, Ross Girshick, Pieter Noordhuis, Lukasz Wesolowski, Aapo Kyrola, Andrew Tulloch, Yangqing Jia, and Kaifeng He. Accurate, large minibatch sgd: Training imagenet in 1 hour. *arXiv preprint arXiv:1706.02677*, 2017.
- Kathleen E. Hamilton, Eugene F. Dumitrescu, and Raphael C. Pooser. Generative model benchmarks for superconducting qubits. *Phys. Rev. A*, 99(6):062323, 2019. arXiv:1811.09905 [quant-ph].
- Tak Hur, Leeseok Kim, and Daniel K. Park. Quantum convolutional neural network for classical data classification. *Quantum Mach. Intell.*, 4(1):3, 2022. arXiv:2108.00661 [quant-ph].

- Yu Jing, Xiaogang Li, Yang Yang, Chonghang Wu, Wenbing Fu, Wei Hu, Yuanyuan Li, and Hua Xu. RGB Image Classification with Quantum Convolutional Ansatz. *Quantum Inf Process*, 21(3):101, 2022. arXiv:2107.11099 [quant-ph].
- Peter D. Johnson, Jonathan Romero, Jonathan Olson, Yudong Cao, and Alán Aspuru-Guzik. Qvector: an algorithm for device-tailored quantum error correction, 2017.
- Diederik P. Kingma and Jimmy Ba. Adam: A method for stochastic optimization, 2017.
- Yann LeCun, Léon Bottou, Yoshua Bengio, and Patrick Haffner. Gradient-based learning applied to document recognition. *Proceedings of the IEEE*, 86(11):2278–2324, 1998.
- Lorenzo Leone, Salvatore F.E. Oliviero, Lukasz Cincio, and M. Cerezo. On the practical usefulness of the hardware efficient ansatz. *Quantum*, 8:1395, 2024.
- Alistair Letcher, Stefan Woerner, and Christa Zoufal. Tight and Efficient Gradient Bounds for Parameterized Quantum Circuits, 2024. arXiv:2309.12681 [quant-ph].
- Hong Li, Nan Jiang, Rui Zhang, Zichen Wang, and Hailiang Wang. Quantum Support Vector Machine Based on Gradient Descent. *Int J Theor Phys*, 61(3):92, 2022.
- Zhiyuan Li and Sanjeev Arora. An exponential learning rate schedule for deep learning. *arXiv preprint arXiv:1910.07454*, 2019.
- Daniel A Lidar and Todd A Brun. *Quantum error correction*. Cambridge university press, 2013.
- Junhua Liu, Kwan Hui Lim, Kristin L. Wood, Wei Huang, Chu Guo, and He-Liang Huang. Hybrid quantum-classical convolutional neural networks. *Sci. China Phys. Mech. Astron.*, 64(9):290311, 2021.
- Zidu Liu, Li-Wei Yu, L.-M. Duan, and Dong-Ling Deng. Presence and Absence of Barren Plateaus in Tensor-Network Based Machine Learning. *Phys. Rev. Lett.*, 129(27):270501, 2022. Publisher: American Physical Society.
- Seth Lloyd, Masoud Mohseni, and Patrick Rebentrost. Quantum algorithms for supervised and unsupervised machine learning. *arXiv preprint arXiv:1307.0411*, 2013.
- Ilya Loshchilov and Frank Hutter. Sgdr: Stochastic gradient descent with warm restarts. *arXiv preprint arXiv:1608.03983*, 2016.
- Ian MacCormack, Conor Delaney, Alexey Galda, Nidhi Aggarwal, and Prineha Narang. Branching quantum convolutional neural networks, 2020.
- I.I. Manin. *Vychislimoe I Nevychislimoe*. "Sov. radio", Moskva, 1980.
- Jarrod R McClean, Jonathan Romero, Ryan Babbush, and Alán Aspuru-Guzik. The theory of variational hybrid quantum-classical algorithms. *New Journal of Physics*, 18(2):023023, 2016.
- Nhat A Nghiem, Samuel Yen-Chi Chen, and Tzu-Chieh Wei. A unified framework for quantum supervised learning. *arXiv preprint arXiv:2010.13186*, 2020.
- M.A. Nielsen and I.L. Chuang. *Quantum Computation and Quantum Information: 10th Anniversary Edition*. Cambridge University Press, 2010.
- Jae-Eun Park, Brian Quanz, Steve Wood, Heather Higgins, and Ray Harishankar. Practical application improvement to quantum svm: theory to practice. *arXiv preprint arXiv:2012.07725*, 2020.
- John Preskill. Quantum computing and the entanglement frontier. *arXiv preprint arXiv:1203.5813*, 2012.
- J. Ross Quinlan. Induction of decision trees. *Machine learning*, 1:81–106, 1986.
- Patrick Rebentrost, Masoud Mohseni, and Seth Lloyd. Quantum support vector machine for big data classification. *Physical review letters*, 113(13):130503, 2014.
- Herbert Robbins and Sutton Monro. A stochastic approximation method. *The Annals of Mathematical Statistics*, 22(3):400–407, 1951.
- Matías Roodschild, Jorge Gotay Sardiñas, and Adrián Will. A new approach for the vanishing gradient problem on sigmoid activation. *Progress in Artificial Intelligence*, 9(4):351–360, 2020.
- David E Rumelhart, Geoffrey E Hinton, and Ronald J Williams. Learning internal representations by error propagation, parallel distributed processing, explorations in the microstructure of cognition, ed. de rumelhart and j. mcclelland. vol. 1. 1986. *Biometrika*, 71(599-607):6, 1986.
- Pankaj Saraswat. Supervised machine learning algorithm: A review of classification techniques. *Integrated Emerging Methods of Artificial Intelligence & Cloud Computing*, pages 477–482, 2021.
- M. Schuld and F. Petruccione. *Machine Learning with Quantum Computers*. Springer International Publishing, 2021.
- Maria Schuld, Alex Bocharov, Krysta Svore, and Nathan Wiebe. Circuit-centric quantum classifiers. *Phys. Rev. A*, 101(3):032308, 2020. arXiv:1804.00633 [quant-ph].
- Arsenii Senokosov, Alexandr Sedykh, Asel Saginalieva, Basil Kyriacou, and Alexey Melnikov. Quantum machine learning for image classification. *Mach. Learn.: Sci. Technol.*, 5(1):015040, 2024.
- Kevin Shen, Bernhard Jobst, Elvira Shishenina, and Frank Pollmann. Classification of the Fashion-MNIST Dataset on a Quantum Computer, 2024. arXiv:2403.02405 [quant-ph].

- Mingrui Shi, Haozhen Situ, and Cai Zhang. Hybrid Quantum Neural Network Structures for Image Multi-classification, 2023. arXiv:2308.16005 [quant-ph].
- Sukin Sim, Peter D. Johnson, and Alán Aspuru-Guzik. Expressibility and Entangling Capability of Parameterized Quantum Circuits for Hybrid Quantum-Classical Algorithms. *Advanced Quantum Technologies*, 2(12):1900070, 2019. eprint: <https://onlinelibrary.wiley.com/doi/pdf/10.1002/qute.201900070>.
- Samuel A. Stein, Betis Baheri, Daniel Chen, Ying Mao, Qiang Guan, Ang Li, Shuai Xu, and Caiwen Ding. QuClassi: A Hybrid Deep Neural Network Architecture based on Quantum State Fidelity, 2022. arXiv:2103.11307 [quant-ph].
- Jules Tilly, Hongxiang Chen, Shuxiang Cao, Dario Picozzi, Kanav Setia, Ying Li, Edward Grant, Leonard Wossnig, Ivan Rungger, George H. Booth, and Jonathan Tennyson. The Variational Quantum Eigensolver: A review of methods and best practices. *Physics Reports*, 986:1–128, 2022.
- Farrokh Vatan and Colin Williams. Optimal quantum circuits for general two-qubit gates. *Physical Review A—Atomic, Molecular, and Optical Physics*, 69(3):032315, 2004.
- Leni Ven and Johannes Lederer. Regularization and reparameterization avoid vanishing gradients in sigmoid-type networks, 2021.
- Hai-Rui Wei and Yao-Min Di. Decomposition of orthogonal matrix and synthesis of two-qubit and three-qubit orthogonal gates, 2012. arXiv:1203.0722 [quant-ph].
- Han Xiao, Kashif Rasul, and Roland Vollgraf. Fashion-mnist: a novel image dataset for benchmarking machine learning algorithms. *arXiv preprint arXiv:1708.07747*, 2017.
- Takashi Yamakawa and Mark Zhandry. Verifiable quantum advantage without structure. *Journal of the ACM*, 71(3):1–50, 2024.
- Chen Zhao and Xiao-Shan Gao. Analyzing the barren plateau phenomenon in training quantum neural networks with the ZX-calculus. *Quantum*, 5:466, 2021. Publisher: Verein zur Förderung des Open Access Publizierens in den Quantenwissenschaften.
- Zhikuan Zhao, Alejandro Pozas-Kerstjens, Patrick Rebentrost, and Peter Wittek. Bayesian Deep Learning on a Quantum Computer. *Quantum Mach. Intell.*, 1(1-2):41–51, 2019. arXiv:1806.11463 [quant-ph, stat].
- Jie Zhou, Dongfen Li, Yuqiao Tan, Xiaolong Yang, Yundan Zheng, and Xiaofang Liu. A multi-classification classifier based on variational quantum computation. *Quantum Inf Process*, 22(11):412, 2023.

Boosting the Validity of Multi-Class Quantum Outputs: Living on the Edge

Supplementary Material

6 Optimization Ablation

To ascertain the best optimization strategy before running the full experimental suite, we ran an ablation across two optimizers, four learning rate schedulers, and three learning rates. The two optimizers are standard stochastic gradient descent (SGD), invented by Robbins and Monro (1951), and Adam, invented by Diederik (2014). The learning rate schedulers we tested were an exponential scheduler, as defined by Li and Arora (2019), a cosine scheduler, as defined by Loshchilov and Hutter (2016), a piecewise scheduler, as defined by Goyal et al. (2017), and no scheduler, also called a constant scheduler.

For the exponential scheduler, there were ten total transition steps over the full six epochs, with a decay rate of 0.9. For the cosine scheduler, the number of steps was simply the number of training steps. For the piecewise scheduler, there were three transition steps with scale factors of 0.1 and 0.01.

We first ran all the tests on $K = 3$ with the edge method on the CNN7 block, shown in Tab. 4. To average over all the metrics, we look at the Friedman Rank (F-Rank) of each optimization strategy, which ranks the columns and averages the ranks over the rows (Friedman, 1937). Upon discovering the tie that occurs between the piecewise scheduler and constant scheduler with the Adam optimizer, we opted to run it again. This second run focused on the Adam optimizer and ran on $K = 5$ instead. This test is shown in Tab. 5. As exponential decay with a learning rate of 0.01 ranked best for $K = 5$, and nearly as well as piecewise and constant for $K = 3$, this was chosen as the optimal setup.

Opt	LRS	LR	F-Rank (\uparrow)	Valid			Constant		Simulation	
				A_M	A_m	S (\downarrow)	A_M	A_m	L_r	T
SGD	<i>exp</i>	0.01	8.75	54.23	74.3	328.8	47.03	72.82	56.47	78.35
SGD	<i>exp</i>	0.001	4.5	51.17	69.26	198.0	41.57	63.45	50.15	75.06
SGD	<i>exp</i>	0.0001	2.875	42.11	50.3	53.6	33.52	44.64	41.72	57.68
SGD	<i>cos</i>	0.01	9.0	54.24	74.37	331.2	47.05	72.88	56.45	78.41
SGD	<i>cos</i>	0.001	5.0	51.21	69.35	199.8	41.63	63.63	50.41	74.86
SGD	<i>cos</i>	0.0001	3.125	42.15	50.17	53.6	33.55	44.64	41.42	58.3
SGD	<i>step</i>	0.01	9.5	54.24	74.39	331.0	47.05	72.87	56.45	78.41
SGD	<i>step</i>	0.001	5.125	51.21	69.33	200.0	41.64	63.63	50.43	74.85
SGD	<i>step</i>	0.0001	3.0	42.15	50.15	53.6	33.55	44.63	41.43	58.3
SGD	<i>reg</i>	0.01	9.5	54.24	74.39	331.0	47.05	72.87	56.45	78.41
SGD	<i>reg</i>	0.001	5.125	51.21	69.33	200.0	41.64	63.63	50.43	74.85
SGD	<i>reg</i>	0.0001	3.0	42.15	50.15	53.6	33.55	44.63	41.43	58.3
Adam	<i>exp</i>	0.01	9.0	54.77	69.88	303.2	48.49	68.32	58.06	76.76
Adam	<i>exp</i>	0.001	11.25	55.34	70.53	188.2	48.9	74.19	58.7	78.27
Adam	<i>exp</i>	0.0001	6.75	51.78	71.18	257.2	42.74	65.44	51.92	75.17
Adam	<i>cos</i>	0.01	8.875	54.77	69.92	303.4	48.49	68.32	58.06	76.74
Adam	<i>cos</i>	0.001	11.75	55.35	70.54	188.2	48.9	74.19	58.7	78.27
Adam	<i>cos</i>	0.0001	7.125	51.78	71.2	257.2	42.74	65.43	51.92	75.17
Adam	<i>step</i>	0.01	8.875	54.77	69.92	303.4	48.49	68.32	58.06	76.74
Adam	<i>step</i>	0.001	11.875	55.35	70.54	188.2	48.9	74.19	58.7	78.27
Adam	<i>step</i>	0.0001	7.375	51.78	71.2	257.2	42.74	65.43	51.92	75.17
Adam	<i>reg</i>	0.01	8.875	54.77	69.92	303.4	48.49	68.32	58.06	76.74
Adam	<i>reg</i>	0.001	11.875	55.35	70.54	188.2	48.9	74.19	58.7	78.27
Adam	<i>reg</i>	0.0001	7.375	51.78	71.2	257.2	42.74	65.43	51.92	75.17

Table 4: Ablation with $K = 3$ over optimizers (Opt), learning rate schedulers (LRS), and learning rates (LR). Schedulers used include Exponential Decay *exp*, Cosine Decay *cos*, Piecewise Constant *step*, and Constant *reg*.

7 Full Testing Results

In Tab. 6 and Tab. 7 we include the full spread of metrics on both datasets across all circuits and with both methods. The runs are still averaged over the 5 randomly seeded training runs, the full data of which can be found in the code repository if needed. We present all of this here as a readily available analysis of many common 2-qubit ring setups for comparison and benchmarking. We present circuit diagrams for each block in Sec. 8.

Presented beside K and the block is the number of parameters per block $n\theta$, which can be used for further research inspiration and optimization. The metrics included are the macro accuracy A_M and micro accuracy A_m from both the

Opt	LRS	LR	F-Rank (\uparrow)	A_M	Valid A_m	S (\downarrow)	Constant		Simulation	
							A_M	A_m	L_r	T
Adam	<i>exp</i>	0.01	6.75	55.15	81.16	489.4	27.09	13.04	48.94	83.85
Adam	<i>exp</i>	0.001	3.875	53.74	79.22	398.8	25.26	10.27	45.63	82.83
Adam	<i>exp</i>	0.0001	2.25	42.87	64.14	142.8	15.58	0.87	31.34	72.54
Adam	<i>cos</i>	0.01	6.125	55.13	81.24	484.2	27.05	12.88	48.9	83.82
Adam	<i>cos</i>	0.001	4.875	53.77	79.31	405.0	25.31	10.31	45.69	82.85
Adam	<i>cos</i>	0.0001	3.125	43.01	64.49	144.6	15.67	0.86	31.54	72.69
Adam	<i>step</i>	0.01	6.125	55.13	81.24	484.2	27.05	12.88	48.9	83.82
Adam	<i>step</i>	0.001	4.875	53.77	79.31	405.0	25.31	10.31	45.69	82.85
Adam	<i>step</i>	0.0001	3.125	43.01	64.49	144.6	15.67	0.86	31.54	72.69
Adam	<i>reg</i>	0.01	6.25	55.14	81.23	483.6	27.06	12.79	48.91	83.81
Adam	<i>reg</i>	0.001	4.75	53.78	79.24	403.4	25.31	10.29	45.69	82.84
Adam	<i>reg</i>	0.0001	2.5	43.01	64.41	145.4	15.67	0.86	31.54	72.67

Table 5: Ablation with $K = 5$ using Adam over learning rates (LR), learning rate schedulers (LRS). Schedulers used include Exponential Decay *exp*, Cosine Decay *cos*, Piecewise Constant *step*, and Constant *reg*.

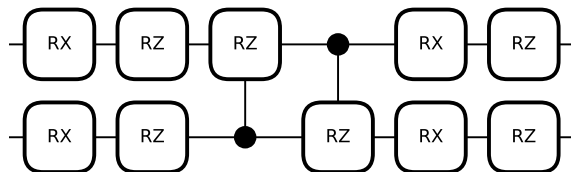


Figure 8: CNN7 Block from Sim et al. (2019), as modified by Hur et al. (2022).

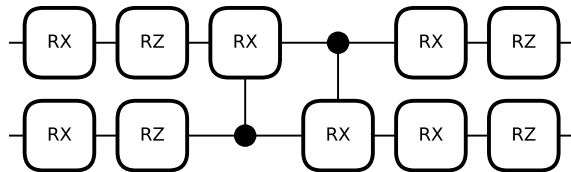


Figure 9: CNN8 Block from Sim et al. (2019), as modified by Hur et al. (2022).

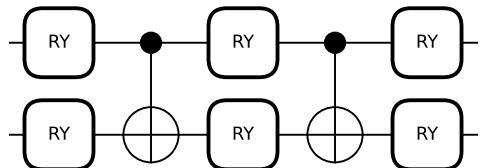


Figure 10: S(O)4 Block from Wei and Di (2012), as modified by Hur et al. (2022).

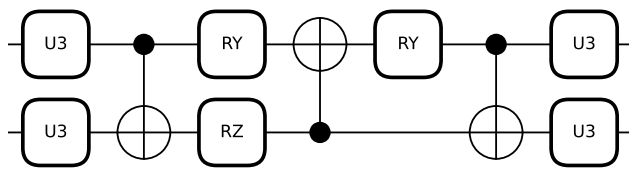


Figure 11: S(U)4 Block from Vatan and Williams (2004), as modified by Hur et al. (2022).

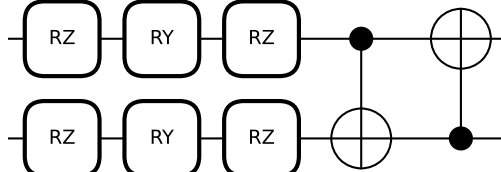


Figure 12: Strongly Entangling Layer Block with CNOT imprimitive (Sel-X) from Schuld et al. (2020).

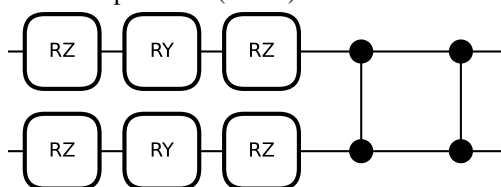


Figure 13: Strongly Entangling Layer Block with CZ imprimitive (Sel-Z) from Schuld et al. (2020).

validity experiment and the constant sampling experiment, the sampling rate S from the validity experiment, as well as the threshold accuracy T and the log-likelihood ratio L_r from the simulation testing. The log-likelihood ratio L_r is computed as the average difference between the highest activation class and the second highest activation class.

The macro accuracies were computed using the trace of the confusion matrices in a similar fashion to the micro accuracies explained in Sec. 4, only this time adding every m-sample to the row corresponding to the target class of each t-sample rather than 1 to the majority vote of the m-samples.

8 QML Block Descriptions

Here we present information about the blocks used in the 2-qubit ring structure. In this section, we will simply summarize the findings of the introductory works to justify their usage in this paper.

The first four of the blocks were found in the work by Hur et al. (2022) and showed promising results in all their experiments. In that paper, the reason each block was chosen was explained succinctly. The CNN7 and CNN8 blocks were first introduced as 4-qubit error-correcting encoders by Johnson et al. (2017). They showed the best expressibility

K	Block	$n\theta$	Method	Valid			Constant		Simulation	
				A_M	A_m	S	A_M	A_m	L_r	T
3	CNN7	10	Edge	58.75	75.57	535.8	55.51	74.25	56.66	76.36
3	CNN7	10	Vertex	63.55	74.56	441.2	39.08	50.19	56.27	76.38
3	CNN8	10	Edge	57.86	75.92	495.2	55.44	75.19	55.78	76.55
3	CNN8	10	Vertex	62.85	74.71	437.4	42.97	59.9	57.48	76.12
3	SO(4)	6	Edge	57.6	73.94	419.8	53.24	73.49	55.26	76.3
3	SO(4)	6	Vertex	60.01	75.32	481.4	30.53	29.55	54.04	76.11
3	SU(4)	15	Edge	58.2	75.39	445.0	54.21	74.71	56.26	76.19
3	SU(4)	15	Vertex	62.13	74.9	449.6	43.37	62.16	56.31	76.22
3	SEL-X	3	Edge	58.03	74.14	440.2	51.79	73.32	56.26	76.35
3	SEL-X	3	Vertex	59.31	75.86	500.0	40.46	57.97	54.82	76.76
3	SEL-Z	3	Edge	56.83	72.69	349.0	48.0	71.73	53.91	76.35
3	SEL-Z	3	Vertex	57.67	75.35	431.2	43.54	70.01	54.17	76.01
4	CNN7	10	Edge	56.12	81.98	883.6	42.73	74.34	52.69	83.32
4	CNN7	10	Vertex	57.88	81.47	832.4	33.4	32.53	56.33	83.95
4	CNN8	10	Edge	57.6	82.57	986.4	43.68	74.67	53.07	84.39
4	CNN8	10	Vertex	58.52	83.45	1084.6	35.11	41.81	57.04	85.01
4	SO(4)	6	Edge	50.56	79.79	618.6	35.76	60.11	42.45	81.8
4	SO(4)	6	Vertex	53.13	80.39	653.4	28.51	19.35	49.69	83.26
4	SU(4)	15	Edge	57.36	81.51	667.4	44.68	75.32	54.35	84.21
4	SU(4)	15	Vertex	58.01	82.82	933.8	36.07	47.26	56.9	85.16
4	SEL-X	3	Edge	48.77	72.71	295.8	32.23	41.51	36.03	80.2
4	SEL-X	3	Vertex	47.41	74.04	296.8	18.79	1.77	38.05	80.84
4	SEL-Z	3	Edge	47.03	64.1	134.6	28.12	29.36	32.03	74.74
4	SEL-Z	3	Vertex	43.44	64.95	156.0	17.58	3.02	32.32	73.92
5	CNN7	10	Edge	59.02	78.93	519.2	31.39	27.93	47.68	81.51
5	CNN7	10	Vertex	52.47	78.65	579.6	21.5	3.55	51.3	82.38
5	CNN8	10	Edge	59.52	79.39	645.8	33.71	35.69	50.05	81.86
5	CNN8	10	Vertex	55.84	80.79	679.6	24.51	8.67	55.68	83.52
5	SO(4)	6	Edge	54.24	75.22	396.2	26.29	16.23	40.27	79.82
5	SO(4)	6	Vertex	48.86	77.38	508.6	19.07	0.58	47.4	81.34
5	SU(4)	15	Edge	59.88	81.32	921.4	33.52	34.97	50.43	83.01
5	SU(4)	15	Vertex	57.08	81.74	711.4	26.54	11.31	56.91	83.98
5	SEL-X	3	Edge	19.56	19.59	10.6	6.13	0.0	0.67	19.39
5	SEL-X	3	Vertex	20.37	20.36	16.2	3.17	0.0	3.76	21.07
5	SEL-Z	3	Edge	48.04	63.08	151.4	19.79	7.41	31.32	70.18
5	SEL-Z	3	Vertex	38.66	58.54	112.0	12.53	0.04	30.96	67.96
6	CNN7	10	Edge	55.12	67.95	275.8	19.77	4.85	38.58	73.06
6	CNN7	10	Vertex	44.2	70.36	292.0	14.06	0.06	45.7	76.42
6	CNN8	10	Edge	58.09	68.02	288.6	21.71	8.59	41.29	75.07
6	CNN8	10	Vertex	45.92	73.21	329.0	15.25	0.53	47.55	78.4
6	SO(4)	6	Edge	51.63	64.26	187.0	14.74	0.66	32.58	70.91
6	SO(4)	6	Vertex	38.43	67.45	204.6	11.17	0.01	39.64	74.79
6	SU(4)	15	Edge	59.34	72.99	342.6	24.18	12.74	43.51	76.39
6	SU(4)	15	Vertex	49.92	76.72	479.2	17.66	0.85	52.39	80.15
6	SEL-X	3	Edge	22.57	24.68	24.2	4.11	0.0	3.72	36.57
6	SEL-X	3	Vertex	20.48	21.42	24.0	2.98	0.0	6.48	35.84
6	SEL-Z	3	Edge	41.88	48.05	64.8	10.42	0.83	24.77	58.74
6	SEL-Z	3	Vertex	28.23	39.54	50.0	7.24	0.0	21.96	52.91

Table 6: Full testing suite results on the MNIST Fashion dataset.

in a study by Sim et al. (2019), leading to them being chosen by Hur et al. (2022). Expressibility, in the context of QML, is a measure of the ability of a circuit to produce a wide range of quantum states.

The SO(4) block was shown by Wei and Di (2012) to be able to implement an arbitrary SO(4) operation, and can be used to construct a fully entangled VQE. The SU(4) block was shown by Vatan and Williams (2004) and MacCormack et al. (2020) to be able to implement any arbitrary 2-qubit rotation.

Strongly Entangling Layers is a popular multi qubit gate-operation that is available as a callable function in the popular quantum computing package PennyLane (Bergholm et al., 2022). The setup was invented in a paper by several of the authors responsible for the creation of PennyLane in Schuld et al. (2020), and has seen much use due to simplicity and expressibility.

Note that the ring structure for the Strongly Entangling Layers block works a bit differently. All single-qubit operations are applied before the ring of two-qubit operations rather than in alternating full block rings like in CNN7, CNN8, SO(4) and SU(4), as visualized in Fig. 1. We included this block in our analysis so as to demonstrate the efficacy of the edge encoding independent of the 2-qubit ring structure.

K	Block	$n\theta$	Method	Valid			Constant		Simulation	
				A_M	A_m	S	A_M	A_m	L_r	T
3	CNN7	10	Edge	57.01	73.85	315.2	52.43	73.53	55.44	76.77
3	CNN7	10	Vertex	58.74	71.88	304.2	38.45	49.68	54.34	76.4
3	CNN8	10	Edge	57.04	75.47	385.0	52.2	74.45	55.67	77.86
3	CNN8	10	Vertex	58.47	72.83	341.0	39.53	54.05	54.67	76.55
3	SO(4)	6	Edge	49.24	65.78	143.6	42.83	65.13	43.94	70.2
3	SO(4)	6	Vertex	50.17	65.71	138.6	27.17	16.52	43.29	69.1
3	SU(4)	15	Edge	56.58	73.55	333.0	51.63	73.14	55.36	77.32
3	SU(4)	15	Vertex	58.08	72.2	310.6	38.26	52.03	53.74	76.53
3	SEL-X	3	Edge	55.14	72.69	299.6	49.66	72.25	54.43	77.47
3	SEL-X	3	Vertex	59.23	72.86	306.0	36.12	43.43	52.96	76.61
3	SEL-Z	3	Edge	55.34	72.04	296.2	45.39	66.89	49.33	77.09
3	SEL-Z	3	Vertex	58.07	74.2	308.4	40.01	57.57	52.77	75.93
4	CNN7	10	Edge	62.51	88.87	1679.2	45.88	77.15	57.06	89.42
4	CNN7	10	Vertex	63.08	89.18	1921.8	33.29	25.83	60.46	90.44
4	CNN8	10	Edge	64.63	89.74	2053.2	48.13	80.39	59.55	90.6
4	CNN8	10	Vertex	65.35	89.91	2292.4	36.39	35.88	62.94	90.91
4	SO(4)	6	Edge	54.37	83.65	889.0	37.38	60.71	46.35	86.14
4	SO(4)	6	Vertex	56.27	85.08	1078.6	27.49	10.63	51.32	87.79
4	SU(4)	15	Edge	64.34	89.72	2112.2	48.71	81.48	60.49	90.93
4	SU(4)	15	Vertex	65.34	90.46	2509.6	38.44	46.57	64.53	91.44
4	SEL-X	3	Edge	47.84	75.42	323.2	26.91	17.63	29.31	81.26
4	SEL-X	3	Vertex	48.62	76.65	425.0	19.09	2.66	37.33	85.12
4	SEL-Z	3	Edge	53.08	73.79	280.2	31.47	33.68	37.69	79.44
4	SEL-Z	3	Vertex	44.96	69.45	224.4	16.95	0.69	33.8	77.73
5	CNN7	10	Edge	58.29	80.25	463.0	29.25	20.91	42.96	82.64
5	CNN7	10	Vertex	52.3	81.0	532.0	19.67	0.65	48.11	83.71
5	CNN8	10	Edge	60.13	81.54	523.6	31.71	27.27	45.42	83.81
5	CNN8	10	Vertex	54.87	83.76	706.0	22.23	1.89	51.55	85.35
5	SO(4)	6	Edge	51.51	74.01	294.4	22.03	5.63	34.61	78.7
5	SO(4)	6	Vertex	44.7	78.33	443.2	15.81	0.13	39.97	81.92
5	SU(4)	15	Edge	62.39	83.78	690.6	32.67	28.81	48.65	84.97
5	SU(4)	15	Vertex	57.86	85.93	957.8	24.08	4.05	54.23	87.82
5	SEL-X	3	Edge	20.35	20.71	15.4	6.27	0.0	0.69	19.6
5	SEL-X	3	Vertex	20.15	20.01	14.2	3.21	0.0	2.19	15.66
5	SEL-Z	3	Edge	46.18	60.25	107.8	17.64	3.37	28.5	65.83
5	SEL-Z	3	Vertex	31.97	46.6	65.4	10.02	0.01	23.12	57.07
6	CNN7	10	Edge	59.64	73.7	283.0	20.47	4.29	37.75	78.13
6	CNN7	10	Vertex	43.26	72.93	334.0	12.49	0.0	42.18	78.0
6	CNN8	10	Edge	61.4	75.47	324.0	21.66	6.53	40.1	78.64
6	CNN8	10	Vertex	45.27	77.02	385.8	13.66	0.03	44.97	81.51
6	SO(4)	6	Edge	48.79	66.81	181.4	13.47	0.15	26.92	73.71
6	SO(4)	6	Vertex	38.84	72.17	301.2	11.07	0.0	38.14	76.41
6	SU(4)	15	Edge	63.6	77.38	389.0	24.35	8.31	43.02	79.61
6	SU(4)	15	Vertex	52.36	82.97	648.8	17.51	0.28	52.82	84.18
6	SEL-X	3	Edge	19.81	20.43	19.0	3.74	0.0	1.6	28.63
6	SEL-X	3	Vertex	19.41	19.9	23.2	2.62	0.0	4.83	35.32
6	SEL-Z	3	Edge	44.18	49.78	62.0	9.48	0.07	23.16	60.3
6	SEL-Z	3	Vertex	26.58	35.85	43.2	7.04	0.0	19.48	48.29

Table 7: Full testing suite results on the MNIST Digits dataset.

For even greater fairness, we include two versions using the two most common parameter-free 2-qubit operations, namely the CNOT gate and CZ gate. For more information about the gate-operations performed in these blocks, we present an accelerated introduction to quantum computing in Sec. 9.

9 Introduction to Quantum Machine Learning

In this section, we will give a low-level overview of the ideas from quantum computing needed to understand this work. This information is summarized from the works of Nielsen and Chuang (2010) and Schuld and Petruccione (2021) which cover it in much greater detail for the interested reader.

Qubits - Qubits are the quantum equivalent to a bit in classical computing. The state of a qubit is represented as a two dimensional vector in a Hilbert space, with classical states 0 and 1 corresponding to the quantum states $|0\rangle$ and $|1\rangle$, where

$$|0\rangle = \begin{bmatrix} 1 \\ 0 \end{bmatrix}, \text{ and } |1\rangle = \begin{bmatrix} 0 \\ 1 \end{bmatrix}. \tag{7}$$

Unlike classical bits which are binary, the state of a qubit can be any length-1 vector in the two-dimensional complex vector space spanned by $|0\rangle$ and $|1\rangle$.

Gates - Quantum gates are a quantum extension of classical reversible-logic gates.

These transform states unitarily (complex angle-preserving), so correspond to complex rotations. Simple examples include the Pauli-X, Pauli-Y, and Pauli-Z gates, written mathematically as σ_1 , σ_2 and σ_3 , respectively. Pauli-X, Pauli-Y, and Pauli-Z are also names for the cardinal axes within the sphere of all possible states a single qubit can take, the so-called "Bloch sphere". The matrices which represent these operations rotate a qubit π radians around the respective axis, and all of them can be written at once as,

$$\sigma_j = \begin{pmatrix} \delta_{j3} & \delta_{j1} - i\delta_{j2} \\ \delta_{j1} + i\delta_{j2} & -\delta_{j3} \end{pmatrix}. \quad (8)$$

Many other gates exist, including gates to elicit interactions between qubits and parameterized versions of the Pauli Gates which allow rotations of arbitrary degree around their respective axes. The subset used in this work can be found in Fig. 14. A brief description of these is provided, but more comprehensive details, as well as more gates, can be found in the works of Nielsen and Chuang (2010) and Schuld and Petruccione (2021).

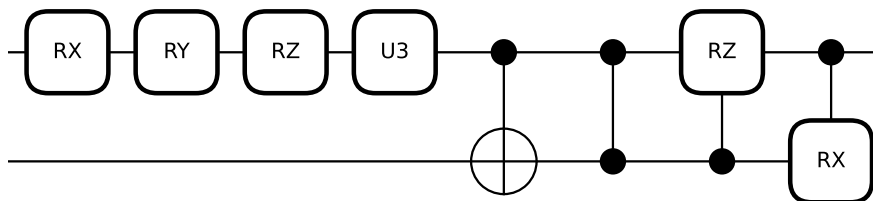


Figure 14: Subset of quantum gates used in the circuits in this paper. From left to right: Pauli-X rotation, Pauli-Y rotation, Pauli-Z rotation, 3-parameter unitary gate, CNOT, CZ, Controlled Pauli-Z rotation, and controlled Pauli-X rotation.

Of these gates, CNOT, CZ, and the controlled Pauli gates all apply their rotations conditionally based on the state of the dotted wire. In the case of the controlled Pauli rotations, this rotation is parameterized, where for CNOT and CZ, it is always a rotation of π radians about the Pauli-X and Pauli-Z axes, respectively. The regular rotation gates are parameterized versions of their Pauli gates. The U3 gate is a special gate which applies a parameterized Pauli-Z, followed by a parameterized Pauli-Y, and then another parameterized Pauli-Z, enabling any arbitrarily Euler rotation about the Bloch Sphere.

Circuits - The term "circuit" typically refers to a more complicated unitary operator built up from a number of quantum gates that are composed sequentially. The term *wire* refers to single qubits as they traverse the different operations within a circuit. The term "model" can often be interchanged with "circuit," though perhaps self-evidently, only when the model can be represented as a circuit.

Measurements - To extract information from a quantum circuit, a measurement of the qubits involved must be performed. A measurement has an associated Hermitian operator (real-valued eigenvalues) where the eigenvalues are the possible outcomes, and the squared length of the state projection onto one of the eigenspaces determines the probability of the corresponding outcome. Due primarily to convention, the most common measurement in quantum computing is measurement in the "computational basis", associated with the Hermitian Pauli-Z operator (Schuld and Petruccione, 2021; Nielsen and Chuang, 2010).

A measurement always gives one of the eigenvalues of the Hermitian operator. For a Pauli-Z measurement we obtain one of two discrete outputs, +1 or -1 (mapped to the bit values 0 or 1, respectively). The *expectation value*, or the expected (average) output is then the weighted average of the outcomes. For a Pauli-Z measurement, this would be

$$E(\sigma_3) = (+1)P(+1) + (-1)P(-1) \quad (9)$$

Note that the range of this expression is $[-1, +1]$ because the eigenvalues of the σ_3 operator are +1 and -1 rather than the binary 0 and 1. If the two outcomes are equally probable, the expectation value here is = 0 rather than = 1/2, which becomes important when setting thresholds in the simulation output.

Such an expectation value can be calculated directly, though this is only possible in simulations. In an actual machine, the outputs would be the discrete values +1 and -1, so to estimate the expectation value when using a quantum computer one would need to count the outcomes and produce a point sample from a series of measurements.

It is important, in the context of this work, to view the expectation value as a measurable quantity output by a quantum model, and not merely a statistic used to describe the quality of said model, without forgetting that it still describes

Living on the Edge

a statistical moment. This ambiguity is a side effect of the collapsing of quantum states, and the disambiguation of these two definitions is part of what makes sample accuracy so important. A model can be deemed accurate if its mean output is higher than a certain threshold, as is the goal of most QML research, but this does not mean that outputs will be precise. A precise model will output correct samples more often than not, which promotes pushing the expected values of a model away from the threshold and also reducing the variance.